

# A Simulation of the Response of a Sounding Temperature Sensor Based on the Combination of a Genetic Algorithm and Computational Fluid Dynamics

Juanjuan Wang, Yajuan Jia\* and Jiangping Nan

Xi'an Traffic Engineering Institute, Xi'an, 710300, China

\*Corresponding Author: Yajuan Jia. Email: JiaYajuan100@163.com

Received: 26 February 2020; Accepted: 09 November 2020

**Abstract:** The present study aims at improving the accuracy of weather forecast by providing useful information on the behavior and response of a sounding temperature sensor. A hybrid approach relying on Computational Fluid Dynamics and a genetic algorithm (GA) is used to simulate the system represented by the bead thermistor and the surrounding air. In particular, the influence of different lead angles, sensor lead length, and lead number is considered. The results have shown that when the length of the lead wire of the bead thermistor is increased, the radiation temperature rise is reduced; when the number of lead wire is four and the angle between the lead wires is  $180^\circ$ , the solar radiation angle has a scarce influence on the radiation temperature rise of the sounding temperature sensor.

**Keywords:** Sounding temperature sensor; genetic algorithm; radiation temperature rise; computational fluid dynamics; bead thermistor

## 1 Introduction

Atmospheric temperature is an important index to express the cold and hot conditions of the atmosphere. It has been widely used in economic construction, national defense and other fields, and plays an important role in urban heat island, global greenhouse effect, El Nino phenomenon and other hot research contents [1].

In recent years, the surface temperature observation technology has attracted much attention and achieved good results. However, if only relying on the surface temperature observation data, it is impossible to accurately and comprehensively explain the factors and trends of global climate change. Therefore, it is necessary for researchers to extend the study of atmospheric temperature change to air observation. The comparative study of the law of annual average temperature change in China from 1970 to 2011 showed that the temperature in most areas of China was on the rise from the ground to 700 hPa. In other words, in this area, with the increase of pressure, the temperature was also increased, and the maximum linear trend coefficient reached  $0.22 \text{ K}/10\text{a}$  [2]. A study on the linear variation of annual mean temperature in the upper air region of North China from 1980 to 2012 showed that the temperature increased  $0.07 \text{ K}$  for every 10 years when the pressure increased above 250 hPa [3]. Some scholars analyzed the temperature changes in the global upper air region from 1958 to 2000 by studying the data of the observation station of the sounding thermometer. The results showed that the temperature changed in the air layer from 1000 to 50 hPa, with the range of  $\pm 0.07 \text{ K}/10\text{a}$ . The comparison of the



This work is licensed under a Creative Commons Attribution 4.0 International License, which permits unrestricted use, distribution, and reproduction in any medium, provided the original work is properly cited.

temperature change of 1000–700 hPa air layer from 1960 to 2000 showed that the temperature change was  $-0.05$  K/10a in the high areas [4]. The relevant reports of satellite observations and radiosonde data sets suggested that, from 1960 to 2015, the global atmospheric temperature in the lower stratosphere and the lower troposphere had changed. The results showed that the global temperature in the lower stratosphere had declined, and the overall temperature in the lower troposphere showed an upward trend [5]. Generally speaking, the average speed of temperature change at high altitude and surface is in the range of  $0.01$ – $0.1$  K/10a. To improve the accuracy of atmospheric temperature observation, it is expected to enhance the accuracy of atmospheric temperature change research by improving the measurement accuracy of bead thermistor sensor.

For minimizing the influence of the radiosonde temperature sensor by the radiation warming, some researchers have done many studies on the radiosonde temperature sensor. The research methods include multi-sensor combination method, low-pressure wind tunnel and empirical estimation method, simplified model calculation method, flight sounding instrument experiment method, and other related methods. However, these methods are difficult to accurately and quantitatively calculate the radiation temperature rise of the sounding temperature sensor in the high air flow environment. Among them, the sounding temperature sensors used include bead thermistor, rod thermistor, spiral wire, thermocouple, and rod thermistor capacitor [6].

At present, the research methods of solar radiation temperature rise are limited by the applicability and the difficulty of experimental technology, so it cannot accurately and quantitatively solve the radiation temperature rise of the sounding temperature sensor in the high-altitude working environment. To solve this problem, computational fluid dynamics (CFD) is used to carry out the simulation experiment of the sounding temperature sensor, thereby obtaining the radiation temperature rise. The relationship between the radiation temperature rise of the bead thermistor and the length, angle and quantity of the lead wire is studied, and the numerical simulation results are fitted by genetic algorithm (GA), thereby obtaining the calculation equation of the radiation temperature rise of the four lead bead thermistor under different solar azimuth and solar height.

## 2 Method

### 2.1 CFD

CFD is a combination of modern hydrodynamics, numerical mathematics, and computer science and a marginal science with strong vitality [7]. It regards the electronic computer as a tool and uses various discrete mathematical methods to carry out numerical experiments, computer simulation, and analysis of various problems in fluid mechanics, thus solving various practical problems. The basic idea of CFD is to replace the continuous physical quantities in space domain and time domain with the set of variable values of finite discrete points. The algebraic equations of physical variable relations of discrete points are established by various discretization mathematical methods. Finally, the algebraic equations are solved numerically to obtain the estimated values of physical variable fields [8].

No matter what state a fluid and what motion it is in, its flow problem must follow the three conservation laws of nature: the law of mass conservation, the law of momentum conservation, and the law of energy conservation. According to the law of conservation of mass, the continuity equation can be obtained.

$$\frac{\partial \rho}{\partial t} + \frac{\partial \rho u}{\partial x} + \frac{\partial \rho v}{\partial y} + \frac{\partial \rho w}{\partial z} = 0 \quad (1)$$

In Eq. (1),  $\rho$  represents density,  $t$  represents time,  $u$ ,  $v$  and  $w$  represent velocity components of velocity vector in  $x$ ,  $y$  and  $z$  directions respectively.

According to the law of momentum conservation, Navier-Stokes(N-S) equation can be obtained.

$$\frac{\partial \rho u}{\partial t} + \frac{\partial \rho u u}{\partial x} + \frac{\partial \rho u v}{\partial y} + \frac{\partial \rho u w}{\partial z} = -\frac{\partial p}{\partial x} + \frac{\partial \tau_{xx}}{\partial x} + \frac{\partial \tau_{yx}}{\partial y} + \frac{\partial \tau_{zx}}{\partial z} + F_x \quad (2)$$

$$\frac{\partial \rho v}{\partial t} + \frac{\partial \rho v u}{\partial x} + \frac{\partial \rho v v}{\partial y} + \frac{\partial \rho v w}{\partial z} = -\frac{\partial p}{\partial y} + \frac{\partial \tau_{xy}}{\partial x} + \frac{\partial \tau_{yy}}{\partial y} + \frac{\partial \tau_{zy}}{\partial z} + F_y \quad (3)$$

$$\frac{\partial \rho w}{\partial t} + \frac{\partial \rho w u}{\partial x} + \frac{\partial \rho w v}{\partial y} + \frac{\partial \rho w w}{\partial z} = -\frac{\partial p}{\partial z} + \frac{\partial \tau_{xz}}{\partial x} + \frac{\partial \tau_{yz}}{\partial y} + \frac{\partial \tau_{zz}}{\partial z} + F_z \quad (4)$$

In Eqs. (2)–(4),  $p$  represents the pressure on the fluid micro element,  $\tau$  represents the component of the viscosity stress on the surface of the micro element due to the molecular viscosity, and  $F_x$ ,  $F_y$  and  $F_z$  represent the volume force on the micro element.

According to the law of energy conservation, Eq. (5) can be obtained:

$$\frac{\partial \rho T}{\partial t} + \frac{\partial \rho u T}{\partial x} + \frac{\partial \rho v T}{\partial y} + \frac{\partial \rho w T}{\partial z} = \frac{\partial}{\partial x} \left( \frac{k}{C_p} \frac{\partial T}{\partial x} \right) + \frac{\partial}{\partial y} \left( \frac{k}{C_p} \frac{\partial T}{\partial y} \right) + \frac{\partial}{\partial z} \left( \frac{k}{C_p} \frac{\partial T}{\partial z} \right) \quad (5)$$

In Eq. (5),  $C_p$  represents the specific heat capacity,  $T$  represents the thermodynamic temperature,  $k$  represents the heat transfer coefficient of the fluid.

Navier-Stokes equations (N-S) can describe the momentum conservation equation of viscous incompressible fluid, which only considers the flow of incompressible fluid. Assuming that the fluid has a constant density and is incompressible, then the above Eqs. (1)–(5) can be simplified. Based on this assumption, the mass equation can be expressed as Eq. (6):

$$\text{div}V = 0 \quad (6)$$

The temperature in the gravitational term can be expressed as Eq. (7):

$$\rho = \rho_c [1 - \alpha(T - T_c)] \quad (7)$$

The Boussinesq assumption is made for the incompressible fluid, and the other physical properties of the fluid are considered to be constant except for the factor of density. N-S equation generalizes the general law of viscous incompressible fluid flow, so it has special significance in fluid mechanics. Its vector form can be expressed as Eq. (6):

$$\rho \left( \frac{\partial V}{\partial t} + (V \cdot \nabla)V \right) = f - \nabla P + \mu \nabla^2 V \quad (8)$$

In rectangular coordinates, it can be rewritten as Eq. (7):

$$\rho \left( \frac{\partial u}{\partial t} + u \frac{\partial u}{\partial x} + v \frac{\partial u}{\partial y} + w \frac{\partial u}{\partial z} \right) = f_x - \frac{\partial P}{\partial x} + \mu \left( \frac{\partial^2 u}{\partial x^2} + \frac{\partial^2 u}{\partial y^2} + \frac{\partial^2 u}{\partial z^2} \right) \quad (9)$$

$$\rho \left( \frac{\partial v}{\partial t} + u \frac{\partial v}{\partial x} + v \frac{\partial v}{\partial y} + w \frac{\partial v}{\partial z} \right) = f_y - \frac{\partial P}{\partial y} + \mu \left( \frac{\partial^2 v}{\partial x^2} + \frac{\partial^2 v}{\partial y^2} + \frac{\partial^2 v}{\partial z^2} \right) \quad (10)$$

$$\rho \left( \frac{\partial w}{\partial t} + u \frac{\partial w}{\partial x} + v \frac{\partial w}{\partial y} + w \frac{\partial w}{\partial z} \right) = f_z - \frac{\partial P}{\partial z} + \mu \left( \frac{\partial^2 w}{\partial x^2} + \frac{\partial^2 w}{\partial y^2} + \frac{\partial^2 w}{\partial z^2} \right) \quad (11)$$

where  $\rho$  is the density of the fluid,  $V$  is the velocity vector,  $P$  is the pressure;  $u, v, w$  is the velocity component of the fluid at the point  $(x, y, z)$  at the moment  $t$ ;  $f = \rho g$ ;  $f$  is the external force on the unit volume of fluid, only considering the gravity here. The constant  $\mu$  is the dynamic viscosity.

Partial differential equation (PDE) is the basic equation used to describe the physical phenomena such as heat transfer and flow of fluid [9]. Generally, it is very complex and even impossible to get the approximate or analytical solution of PDE. Therefore, when solving the control equation, first, discretize the calculation domain specially, and obtain the numerical approximation value of the original continuous system by using the solution value of the discretized equation of the node value of the discretized grid. There are many methods to deduce the discrete equation and calculate the distribution assumption of the strain between the nodes. At present, the finite volume method, the finite element method (FEM), and the finite difference method are the discrete methods frequently used. The finite volume method and FEM are more suitable for the complicated boundary conditions.

In mathematics, FEM is a kind of approximate method for solving boundary value problems of PDEs. When solving, the whole problem area is decomposed, and each sub area becomes a simple part, which is called finite element. In reality, most of the problems are difficult to get accurate solutions, while FEM not only has high calculation accuracy, but also can adapt to a variety of complex shapes, so it has become an effective engineering analysis method [10].

As a common numerical algorithm in CFD, the finite volume method is based on the conservation equation of integral form rather than differential equation, which describes each control body defined by computational grid [11]. The finite volume method focuses on the construction of discrete equations from the physical point of view. Each discrete equation is the expression of conservation of some physical quantity on the finite volume. The physical concept of the derivation process is clear, and the coefficient of the discrete equation has certain physical significance and can ensure that the discrete equation has the characteristics of conservation. Dai et al. realized the numerical solution of flow field change through the finite volume method [12].

The resistance body of bead thermistor is an ellipsoid or sphere obtained by ceramic sintering. White paint, high-reflectivity aluminum film, and insulation protection layer are used to wrap the resistance body, and the end of the resistance body is connected with two metal leads wrapped by insulation layer [13,14]. Nowadays, as sensor manufacturing becomes more advanced, the diameter of bead thermistor in the world's top level can be reduced to less than 1 mm. Compared with the traditional sensor bead thermistor, it has a certain advantage in volume, can effectively improve the cooling effect of the sounding temperature sensor, and can reduce the amount of solar radiation absorption, so it has been widely used in the field of high-altitude temperature detection [15,16]. Hence, the bead thermistor is taken as the research object, and the difference between the atmospheric temperature and the bead thermistor is used to describe the radiation temperature rise. The physical characteristics of the components of the sensor shall be considered when calculating the radiation temperature rise, as shown in Tab. 1.

**Table 1:** Physical parameters of each component of bead thermistor

Parts	Density ( $\text{kg}\cdot\text{m}^3$ )	Specific heat capacity ( $\text{J}\cdot\text{kg}^{-1}\cdot\text{k}^{-1}$ )	Thermal conductivity ( $\text{W}\cdot\text{m}^{-1}\cdot\text{k}^{-1}$ )
Thermistor crystal	3900	840	35
Insulating layer	2500	790	0.2
Lead wire	8385	449	86

## 2.2 Model Construction

The components of the bead thermistor are connected by welding, the thickness of the welding position is uneven, and the calculation of the specific numerical value of the connection position is too difficult, which will affect the calculation of the bead thermistor. Therefore, it is necessary to improve the measurement accuracy of the sensor. Before establishing the model, it is assumed that the welding materials between the components of the bead thermistor model are ignored, and the welding between different components is uniform and there is no gap.

Since the working environment of the bead thermistor is the air layer, it is difficult to build a real air model to simulate the infinite air region. After considering the workload and calculation accuracy, an air region with proper size is built around the sensor. Fig. 1 shows the physical model of air region and bead thermistor. The left and right sides of the air area are the air flow outlet and inlet, respectively. Because the heat dissipation effect of the sensor will be greatly reduced in the low-pressure high-altitude environment, the model constructed lengthens the length of the air region in the convection direction, so that the radiation heat absorbed by the sensor can be effectively dissipated.

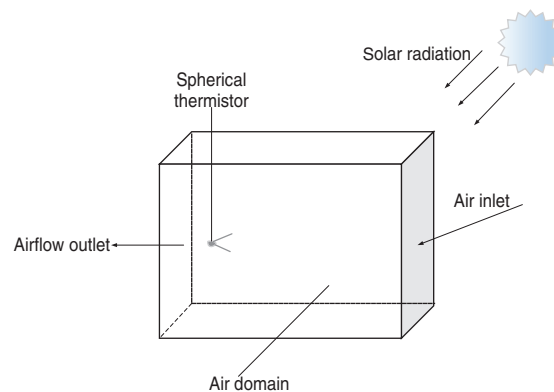


**Figure 1:** Physical model of bead thermistor and peripheral air region

In the model, the external radiation coupling boundary condition is expressed by heat flux density, the solar radiation loading model is adopted, and the radiation intensity is  $1367 \text{ W/m}^2$ . The velocity inlet condition is adopted for the calculation of fluid inlet, and the fluid velocity, temperature and corresponding turbulence conditions are given: The pressure outlet boundary condition is adopted for the outlet. Assuming that the air basin around the bead thermistor is an incompressible gas, the pressure-based solver can be used and the steady flow calculation can be used. In the model, energy equation is used because of radiation heat transfer, convection heat transfer, and heat conduction calculation; laminar flow model is used for turbulent viscosity; SIMPLE algorithm is used for pressure and velocity solution [17,18]. First, the first-order upwind scheme is used to converge the results, and then the second-order upwind scheme is used to improve the accuracy of the results.

The Simple algorithm is a numerical method for solving incompressible flow field, which is also used to solve the compressible flow. Its core is to adopt the “guess-correct” process. The basic idea of Simple algorithm is: For a given pressure field (it can be an assumed value or the result of the last iteration), the momentum equation in discrete form is solved to obtain the velocity field. As the pressure field is assumed or imprecise, the velocity field obtained in this way generally does not satisfy the continuous equation. Therefore, the given pressure field must be corrected. The correction principle is that the velocity field corresponding to the modified pressure field can satisfy the discrete form of continuous

equation at this iteration level. According to this principle, the relation between pressure and velocity specified by the discrete form of momentum equation is substituted into that of continuous equation, thus obtaining the pressure correction equation, and then obtaining the pressure correction value from the pressure correction equation. Then, according to the corrected pressure field, a new velocity field is obtained. Then, check whether the velocity field converges. If not, use the corrected pressure value as the given pressure field to start the next level calculation until it converges.

### **2.3 Numerical Simulation Method**

The CFD software FLUENT is used for numerical simulation. FLUENT is the current international mainstream CFD software and a tool for solving fluid flow and heat transfer problems. Through FLUENT simulation analysis, the heat transfer of bead thermistor is analyzed. After 70 steps of iterative calculation, the convergence is achieved. For steady-state calculation, the convergence index of FLUENT is listed as follows:

(1) The residual meets the requirements. The convergence index of specific parameters is: Energy equation:  $10^{-6}$ ; radiation equation:  $10^{-6}$ ; component equation:  $10^{-5}$ ; other parameters:  $10^{-3}$ . (2) The physical quantities (velocity, temperature, and pressure) of the sensitive positions in the calculation do not continue to change with the iteration. (3) The physical quantities (velocity, temperature, and pressure) at the outlet do not continue to change with the iteration. (4) The mass and energy conservation of the calculation results. (5) The calculation results are independent of the grid, that is, for the results obtained by using a grid, the grid is encrypted and then calculated again, and the results remain the same. (6) The independence of near-wall treatment. (7) Independence of import boundary conditions [19].

### **2.4 Mesh Division of Model**

In the calculation of PDE, the related equation should be discretized first to get the discrete equation which can calculate the result. Therefore, mesh division means discretizing the related equations and obtain the corresponding discrete equations. Because there are many parts in the three-dimensional model of the bead thermistor sensor, and some parts of the structure are irregular, if hexahedral mesh is used, it is difficult to get the convergence results. Consequently, unstructured tetrahedral mesh with strong adaptability is used for mesh division. For improving the accuracy of the numerical simulation results and accurately grasping the conditions of the sensor components and the coupling boundary atmosphere, the small size position of the sensor, the temperature measurement components, and the fluid structure coupling boundary are encrypted. To make the optimization program have automatic mesh generation and numerical calculation, it is necessary to convert the input geometric dimensions into model data that can be recognized by the meshing software through parametric modeling, and then mesh the established three-dimensional model and investigate the grid independence, thereby ensuring the quality of the grid and reducing the number of meshes as far as possible.

According to the above requirements, the physical model of bead thermistor is meshed by ICEMCFD, and 800,000 meshes are divided. ICEMCFD is used for modeling and grid division, and the software will automatically generate user operation log files. Then, the design parameters to be optimized are associated with the corresponding command-line data in the log file. Different values of design variables for each individual will generate different log files. According to the batch command, the software will automatically update the reactor geometry model the next time when the log file is re-read. Although the geometry of the reactor will change according to different design parameters in the optimization process, the overall structure will not change. Hence, different individuals share the same topology in the meshing process, and their geometric models can realize automatic correlation mapping to generate different meshes.

According to the mesh quality criteria of ICEMCFD, the ratio of the maximum matrix to the minimum Jacobian matrix determinant of mesh element cannot be negative, so the mesh quality is more than 0.2.

Through the mesh quality test, the ratio parameters obtained are all higher than 0.36, as shown in Fig. 2. It proves that the mesh quality meets the requirements of numerical calculation, and simulation experiments can be carried out on it.

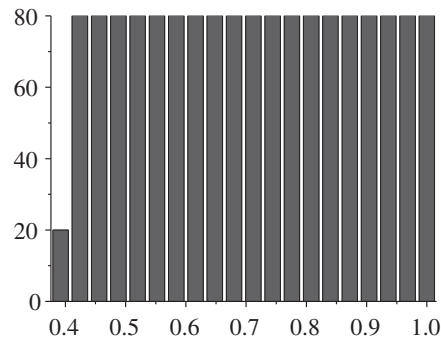


**Figure 2:** Mesh quality distribution

Increasing the grid resolution in a certain range can improve the calculation accuracy, but it needs to pay a large calculation cost to improve the calculation accuracy after exceeding a certain limit value. Analyzing the grid sensitivity can distinguish whether the CFD calculation result depends on the grid quality to seek the balance point of the calculation accuracy and cost, which is an important step to ensure the correctness and efficiency of the CFD model. To balance the calculation time and the accuracy of the results, the grid with the scale of size function of 1:1.2 is used as the calculation grid. Tab. 2 shows the specific selection of calculation grid.

**Table 2:** Selection of calculation grid

Grid type	Size function	Total number of units before conversion to polyhedra	Total number of cells after conversion to Polyhedra
Dense grid	1: 1.1	2307036	592645
Medium grid	1: 1.2	1441518	458778
Sparse grid	1: 1.3	1246059	409138

## 2.5 Radiation Heating Equation

GA is a random parallel search algorithm which combines gene genetics and natural selection. When using GA, it is unnecessary to know the characteristics of the problem to be solved. GA obtains different chromosomes through evaluation algorithm, and implements chromosome screening according to different fitness values of chromosomes, thereby making more adaptable chromosomes multiply in large numbers [20].

CFD can only calculate the finite discrete value model. For example, the numerical simulation results of the temperature field can be obtained under any solar radiation azimuth and solar radiation altitude angle, and then the measurement values of the sounding temperature sensor can be calculated under various environmental conditions. GA is used to fit the simulation results of bead thermistor with 180° lead angle.

In the process of elimination and selection, GA takes the root mean square error  $Re$  as the objective function Eq. (1):

$$Re = \sqrt{\frac{\sum_{i=1}^n (\Delta T_i - \Delta T_i(\beta, \eta))^2}{n}} \quad (13)$$

$\Delta T_i$  is the actual simulation result,  $\Delta T_i(\beta, \eta)$  represents the solution of the radiation temperature rise with respect to the solar azimuth angle  $\eta$  and altitude angle  $\beta$ . Because in equation fitting, the value with larger competition result will be eliminated, and the value with smaller competition result will be saved, the relationship between fitness function and objective function is shown in Eq. (2):

$$F = \frac{1}{Re} \quad (14)$$

The initial population number is set to 200; using uniform crossover method and roulette selection method, the crossover rate is 0.85, and the mutation rate of uniform mutation operator is 0.01. The relationship between the solar azimuth  $\eta$  and altitude angle  $\beta$  and the radiation temperature rise is obtained Eq. (3).

$$\Delta T = \frac{p_1 + p_2 * \beta + p_3 * \beta^2 + p_4 * \eta + p_5 * \eta^2}{1 + p_6 * \beta + p_7 * \beta^2 + p_8 * \eta + p_9 * \eta^2} \quad (15)$$

$p_1 = 1.51185$ ,  $p_2 = 0.02064$ ,  $p_3 = 0.00015$ ,  $p_4 = -0.0587$ ,  $p_5 = 0.00065$ ,  $p_6 = 0.0101$ ,  $p_7 = 0.00015$ ,  $p_8 = -0.0384$ , and  $p_9 = 0.00043$ .

## 2.6 Simulation Experiment

### 2.6.1 Lead Length

Because the sensor bracket will cause radiation temperature rise under the sun irradiation, the heat generated will be transferred to the bead thermistor, resulting in temperature measurement error, so a longer sensor lead should be selected. However, the increase of the lead length will lead to the deterioration of its structural strength, which will make it more vulnerable to air resistance, gravity, and other factors when measuring air temperature.

To study the relationship between the radiation temperature rise of the sensor and the length of the lead wire, the fluid structure coupling multi-physical field simulation experiment of the sensor with different lead wire length is carried out by CFD. In order to reflect the results more directly, the direction of the most sufficient solar radiation to the sensor, that is, the direction of the solar square angle of  $90^\circ$  and the height angle of  $0^\circ$ , is selected. The altitude is set as 32 km, the solar radiation intensity is  $1367 \text{ W/m}^2$ , the reflectivity of the sensor surface coating is 0.8, the physical parameters are the same as Tab. 1, and the lead length is 5–50 mm.

### 2.6.2 Lead Angle

According to the relevant data research, when the altitude is 32 km, the change of the azimuth angle and altitude angle of the solar radiation will lead to the change of the radiation temperature rise of the sensor, and the change range is 0.8 K [21]. When the sounding temperature sensor rises from the ground to the high area, it may rotate or swing, which will make the solar azimuth and altitude angle changed. Restricted by power consumption, volume, and weight on the sounding temperature sensor, the sounding temperature sensor cannot be equipped with the attitude measurement sensor system, which makes the correction of measurement results and calculation of radiation temperature rise more difficult. If a sensor structure which is less affected by the solar radiation angle is found, the influence of the solar radiation angle change on the radiation warming can be minimized, thereby improving the detection accuracy of the radiosonde.

To study the relationship between the solar radiation angle and the radiant temperature rise of the bead thermistor, as shown in Fig. 3, a solar radiation model is proposed. The z-axis is the zenith direction,  $\eta$  is the solar azimuth,  $\beta$  is the solar height angle, and  $\zeta$  is the lead angle.

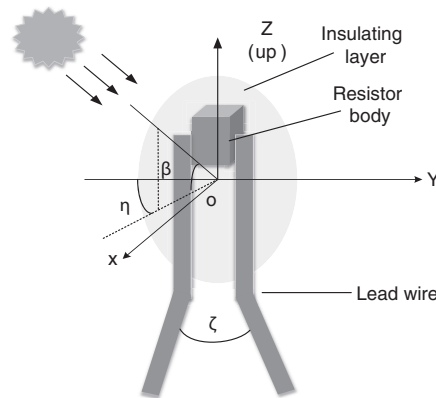


**Figure 3:** The solar radiation model of bead thermistor

CFD is used to simulate the bead thermistor under the condition of different lead angles and solar height angles. The solar azimuth angle is  $0^\circ$ , the altitude is 32 km, the solar radiation intensity is  $1367 \text{ W/m}^2$ , the reflectivity of the sensor surface coating is 0.8, the physical parameters are the same as Tab. 1, and the lead length is 5 mm. The solar altitude angle  $\beta$  is  $0^\circ$ – $90^\circ$  and the step size is  $10^\circ$ . Fig. 6 shows the curve of radiation temperature rise.

It can be seen from Fig. 6 that the radiation temperature rise of the sensor with different lead angles is affected by the solar height angle differently, and the influence is greatly different. When the angle between the leads is zero, the maximum difference of radiation temperature rise is 0.905 K; when the angle between the leads is  $180^\circ$ , the minimum difference of radiation temperature rise is 0.11 K. Through comparative study, when the solar height angle increases from  $0^\circ$  to  $90^\circ$ , the irradiation area of the whole bead thermistor is basically unchanged, the irradiation area of the package surface decreases, the irradiation area of the lead surface increases, and the final solar radiation temperature rise is gradually stable. To sum up, when the solar azimuth angle is  $90^\circ$ , the irradiation area of the package surface and the lead decreases gradually, and the change range of the solar radiation temperature increases gradually. The model of bead thermistor with  $90^\circ$  solar azimuth is simulated. The change range of solar altitude angle is set as  $0^\circ$ – $90^\circ$  and the step size is  $10^\circ$ .

### 2.6.3 Lead Quantity

The interference of  $\eta$  to the radiation temperature rise of bead thermistor should be minimized. According to the symmetry of the lead about the OZ axis and the change rule of the azimuth angle, the relationship between the radiation heating amount and the azimuth angle is studied. To improve the symmetry of the simulation model, the bead thermistor with six leads, four leads, and two leads structure is proposed. The radiation temperature rise of bead thermistor with three structures in the YOZ plane and XOZ plane under different conditions is studied.

## 3 Results

### 3.1 Analysis of Simulation Results

The sensor is welded on the sensor bracket to measure the atmospheric temperature at high altitude. Due to the different structures of each bracket, the lead of bead thermistor is usually arranged into various states.

The numerical simulation experiments of bead thermistor in different states are carried out, and the radiation temperature rise of bead thermistor is analyzed and solved. When the air temperature is measured by the sounding thermometer, it rises from the ground to 32 km air layer at the speed of 6 m/s. In the air region with low altitude, the air pressure is relatively high, the air convection effect is strong, and the heat dissipation effect of the sensor is relatively good. With the rise of altitude, the air pressure decreases, the air convection effect decreases, and the heat dissipation effect of the bead thermistor also decreases. It will seriously affect the calculation of the radiation temperature rise of the sensor. Hence, before the simulation experiment, the relationship between different altitude and air pressure should be mastered. According to the atmospheric model, the increase of altitude will cause the decrease of air pressure through three orders of magnitude, as shown in Fig. 4.

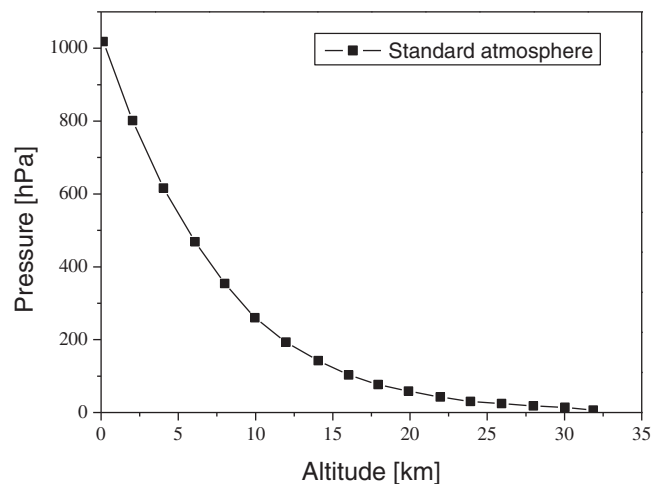


**Figure 4:** Air pressure at different altitudes

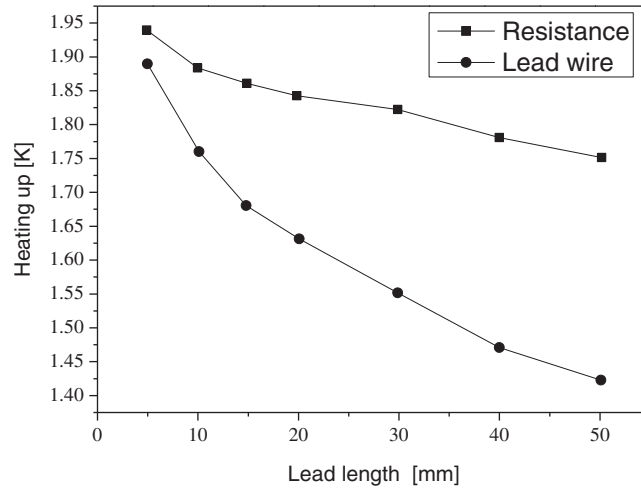
### 3.1.1 Analysis of Lead Length

Fig. 5 shows the relationship between the radiation temperature rise of the sensor and the lead length. According to the simulation results in Fig. 5, it can be found that the radiation temperature rise of the lead and the bead thermistor decreases with the increase of the lead length. When the length of lead wire is 5 mm, the radiation temperature rise of thermistor is 0.19 K higher than that of 50 mm, and the radiation temperature rise of lead wire is 0.47 K higher. In conclusion, it is found that increasing the lead length is beneficial to the heat dissipation of the sensor, thus reducing the influence of the temperature rise of the bead thermistor on the measurement results.

### 3.1.2 Analysis of Lead Angle

It can be seen from Fig. 6 that the radiation temperature rise of the sensor with different lead angles is affected by the solar height angle differently, and the influence is greatly different. When the angle between the leads is zero, the maximum difference of radiation temperature rise is 0.905 K; when the angle between the leads is 180°, the minimum difference of radiation temperature rise is 0.11 K. Through comparative study, when the solar height angle increases from 0° to 90°, the irradiation area of the whole bead thermistor is basically unchanged, the irradiation area of the package surface decreases, the irradiation area of the lead surface increases, and the final solar radiation temperature rise is gradually stable. To sum up, when the solar azimuth angle is 90°, the irradiation area of the package surface and the lead decreases gradually, and the change range of the solar radiation temperature increases gradually. The model of bead thermistor

with 90° solar azimuth is simulated. The change range of solar altitude angle is set as 0°–90° and the step size is 10°. Fig. 7 shows the temperature rise curve.



**Figure 5:** The relationship between radiation temperature rise of sensor and lead length

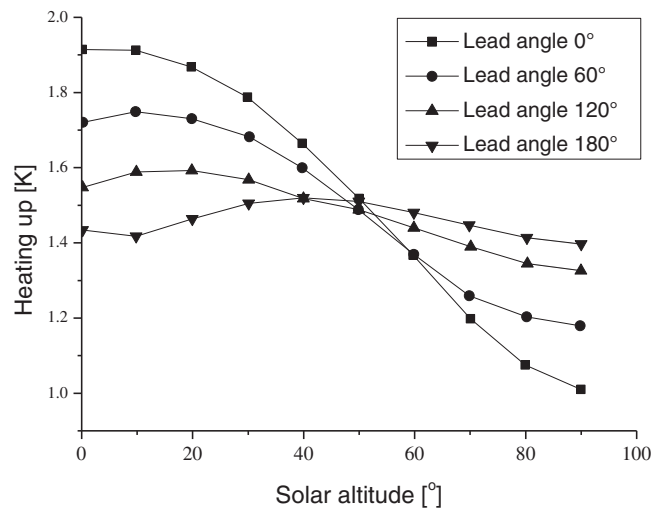


**Figure 6:** The relationship between the radiation temperature rise of the sensor and the angle between the leads

The numerical simulation results in Fig. 7 suggest that when  $\eta$  is 90°, different solar height angles have a very important impact on the radiation temperature rise, and 180° angle has the best stability. It can be concluded that the solar azimuth has a very obvious effect on the temperature detection results, and the 180° lead angle is the best choice.

### 3.1.3 Analysis of Lead Quantity

The numerical simulation results in Fig. 8 show that the radiation temperature rise curve of the four-lead structure in the YOZ plane and XOZ plane is the highest fitted, and the radiation heating curve of the two-lead structure is the lowest. Therefore, it can be concluded that the increase of the number of bead thermistor leads can reduce the influence of solar azimuth on the radiation temperature rise of the sensor.

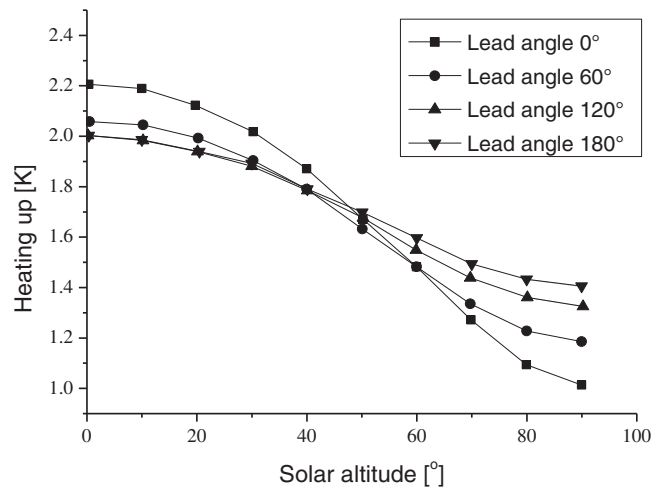


**Figure 7:** The radiant temperature rise of the bead thermistor

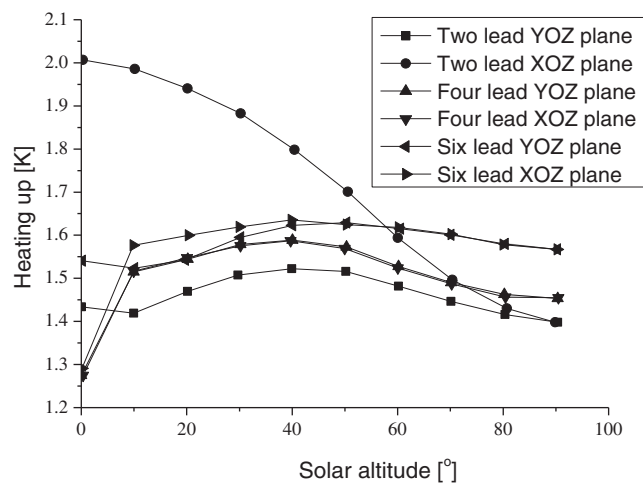


**Figure 8:** Radiation temperature rise of bead thermistor with three lead numbers at different solar altitudes

To further study the influence of the number of leads on the radiation temperature rise and the stability of the radiation temperature rise under other  $\eta$  conditions, the numerical simulation of three kinds of lead bead thermal sensors in different  $\eta$  is carried out in a fluid solid coupling multi-physical field. The variation range of solar azimuth angle and altitude angle was  $0^\circ$ – $90^\circ$  and the step size was  $10^\circ$ . The simulation results suggest that when considering the impact of  $\eta$  and  $\beta$  on the radiosonde temperature of the sensor, the temperature rise of the two-lead temperature sensor changes the greatest, which can reach 0.602 K; the change of the four-lead structure is the smallest, which is 0.226 K; the six-lead structure is 0.36 K, and the mean square deviation is 0.178 K, 0.063 K, and 0.098 K, respectively. To sum up, among the three types of leads, the solar radiation temperature rise has the best coincidence when the number of leads is 4, which is the best choice. If  $\eta$  and  $\beta$  are ranged  $0^\circ$ – $90^\circ$ , and the average temperature rise is 1.536 K as the reference value, the temperature rise can be obtained when the solar irradiation angle cannot be measured, and the measurement accuracy can reach  $\pm 0.113$  K.

### 3.2 Calculation Results of Radiation Temperature Rise

Select the points with sun azimuth angle and altitude angle of 20°, 60° and 90°, respectively for simulation experiment. The simulation result of radiation temperature rise is T1, and the calculation result of radiation temperature rise is T2. The comparison results of the two are shown in [Tab. 3](#).

**Table 3:** Comparison between simulation value and equation calculation value

$\beta/^\circ$	$\eta/^\circ$	T <sub>1</sub> K	T <sub>2</sub> K	T <sub>1</sub> -T <sub>2</sub> K
20	20	300.101	300.093	0.008
20	60	300.146	300.157	-0.011
20	90	300.096	300.105	-0.009
60	20	300.112	300.130	-0.018
60	60	300.087	300.067	0.020
60	90	300.128	300.147	-0.019
90	20	299.987	299.981	0.007
90	60	299.976	299.978	-0.002
90	90	299.981	299.978	0.003

According to [Tab. 3](#), the average error between the simulation value and the calculated value of the equation is 0.011 K. Hence, it is considered that the results of the fitting equation are in good agreement with the results of numerical analysis. It is proved that the equation of radiation temperature rise obtained by GA fitting the simulation results has a good calculation accuracy.

## 4 Discussion

The diameter of the bead thermistor temperature sensor is only 1 mm and the diameter of the lead wire is only 0.02 mm, so the air flow around the sensor is approximately laminar. Under the same altitude, air flow velocity, and solar radiation intensity, theoretically, the temperature rise of the sensor caused by solar radiation is approximately linear with the heating power of absorbing solar radiation, and approximately linear with the projection area of the solar radiation sensor [22]. When the solar height angle increases from 0° to 90°, the projected solar radiation area of the bead thermistor leads with the included angle of 180° leads increases continuously, while the irradiated area of the package decreases continuously, and the change of the overall projected area is small. It can be predicted that the temperature measurement results fluctuate little and the accuracy is high. When the number of leads increases, the symmetry degree of the sensor about the OZ axis increases, the influence of the change of solar azimuth on the radiation projection area decreases, and the fluctuation amplitude of the temperature measurement results of the sensor also decreases. The projection area of the four-lead bead thermistor with 180° lead angle is the least affected by the solar irradiation angle among several sensor shapes with different lead angles and lead numbers. Therefore, according to the theoretical analysis, it should have the relatively highest temperature measurement accuracy [23]. The numerical simulation results in [Figs. 5–8](#) are consistent with the theoretical analysis conclusion, and also with the research results of Yang et al. [24].

## 5 Conclusion

The simulation experiment of the sounding temperature sensor is carried out by using CFD and GA. It is found that the radiation temperature rise of the bead thermistor will decrease with the increase of its lead length. When the number of leads is four and the angle between the leads is 180°, the solar radiation

angle has the least influence on the radiation temperature rise of the sounding temperature sensor. Based on GA, the calculation equation of radiation temperature rise which is consistent with the numerical analysis results is obtained. However, only one kind of radiosonde temperature sensor working environment is simulated and the equation is fitted. In the next step, the radiation temperature rise under various solar radiation conditions and altitude will be further discussed.

**Funding Statement:** The author(s) received no specific funding for this study.

**Conflicts of Interest:** The authors declare that they have no conflicts of interest to report regarding the present study.

## References

- Horton, D. E., Johnson, N. C., Singh, D., Swain, D. L., Rajaratnam, B. et al. (2015). Contribution of changes in atmospheric circulation patterns to extreme temperature trends. *Nature*, 522(7557), 465–469. DOI 10.1038/nature14550.
- Arrif, T., Chehhat, A., Abo-Serie, E., Benchabane, A. (2018). Numerical study of natural convection in square tilted solar cavity considering extended domain. *Fluid Dynamics & Materials Processing*, 14(4), 223–242. DOI 10.32604/fdmp.2018.01799.
- Chen, R., Yin, P., Meng, X., Liu, C., Wang, L. et al. (2017). Fine particulate air pollution and daily mortality: A nationwide analysis in 272 Chinese cities. *American Journal of Respiratory and Critical Care Medicine*, 196(1), 73–81. DOI 10.1164/rccm.201609-1862OC.
- Li, X., Chen, L., Guo, A., Su, L., Zhang, Y. (2015). Sub-millimeter wave limb sounding simulation of the plume flow of a high-flying vehicle. *Journal of Remote Sensing*, 19(1), 54–61.
- Jansen, M. (2017). Glacial ocean circulation and stratification explained by reduced atmospheric temperature. *Proceedings of the National Academy of Sciences of the United States of America*, 114(1), 45–50. DOI 10.1073/pnas.1610438113.
- Kadygrov, E. N., Ganshin, E. V., Miller, E. A., Tochilkina, T. A. (2015). Ground-based microwave temperature profilers: potential and experimental data. *Atmospheric and Oceanic Optics*, 28(6), 598–605. DOI 10.1134/S102485601506007X.
- Dandani, M., Lepiller, V., Ghezal, A., Desevaux, P. (2018). Numerical visualizations of mixing enhancement in a 2d supersonic ejector. *Fluid Dynamics and Materials Processing*, 14(1), 23–37.
- Azoui, H., Bahloul, D., Soltani, N. (2018). Three-dimensional numerical investigation of convective thermal instabilities in the sapphire melt for czochralski growth process. *Fluid Dynamics & Materials Processing*, 14(2), 87–105.
- Md, S., Narayana, P. V. S. (2018). Primary and secondary flows on unsteady MHD free convective micropolar fluid flow past an inclined plate in a rotating system: A finite element analysis. *Fluid Dynamics and Materials Processing*, 14(1), 57–86.
- Neffah, Z., Kahalerras, H., Fersadou, B. (2018). Heat and mass transfer of a non-newtonian fluid flow in an anisotropic porous channel with chemical surface reaction. *Fluid Dynamics and Materials Processing*, 14(1), 39–56.
- Slama, S., Kahalerras, H., Fersadou, B. (2017). Mixed convection of a nanofluid in a vertical anisotropic porous channel with heated/cooled walls. *Fluid Dynamics & Materials Processing*, 13(3), 155–172.
- Wang, Z., Dong, K., Zhan, S. (2017). Numerical analysis on unsteady internal flow in an evaporating droplet. *Fluid Dynamics & Materials Processing*, 13(4), 221–234.
- Yusha, V. L., Busarov, S. S., Goshlya, R. Y., Nedovenchanyi, A. V., Busarov, I. S. (2016). The Experimental research of the thermal conditions in slow speed stage of air reciprocating compressor. *Procedia Engineering*, 152, 297–302. DOI 10.1016/j.proeng.2016.07.706.
- Maksimovic M., Vujovic V., Perisic B., Milosevic V. (2015). Developing a fuzzy logic based system for monitoring and early detection of residential fire based on thermistor sensors. *Computer Science and Information Systems*, 12(1), 63–89. DOI 10.2298/CSIS140330090M.

15. Metawa, N., Hassan, M. V. K., Elhoseny, M. (2017). Genetic algorithm based model for optimizing bank lending decisions. *Expert Systems with Applications*, 80, 75–82. DOI 10.1016/j.eswa.2017.03.021.
16. Korenbaum, V., Shiryaev, A. (2015). The features of sound propagation through human lungs, revealed by transmission sounding with phase manipulated acoustic signal of 80-1000 Hz frequency band. *Journal of the Acoustical Society of America*, 137(4), 2424. DOI 10.1121/1.4920840.
17. Jiang, S., Fu, S. (2018). Modifications to the SIMPLE algorithm with the MDCD approach for incompressible flow simulation. *International Journal of Numerical Methods for Heat & Fluid Flow*, 28(9), 2208–2230. DOI 10.1108/HFF-02-2018-0054.
18. Suthakar, K., Liberman, M. C. (2019). A simple algorithm for objective threshold determination of auditory brainstem responses. *Hearing Research*, 381, 107782. DOI 10.1016/j.heares.2019.107782.
19. Li, J., Qin, Z., Liu, G. (2016). A new generation of Chinese FY-3C microwave sounding measurements and the initial assessments of its observations. *International Journal of Remote Sensing*, 37(17), 4035–4058. DOI 10.1080/01431161.2016.1207260.
20. Qin, S., Ma, Z., Jiang, C., Lin, J., Xue, Y. et al. (2017). Response characteristics and experimental study of underground magnetic resonance sounding using a small-coil sensor. *Sensors*, 17(9), 2127. DOI 10.3390/s17092127.
21. Pan, G., Xu, X., Zhang, X. (2017). On the relationship between the QBO/ENSO and atmospheric temperature using COSMIC radio occultation data. *Journal of Atmospheric and Solar-Terrestrial Physics*, 156, 103–110. DOI 10.1016/j.jastp.2017.03.008.
22. Han, S., Liu, Q., Han, X., Dai, W., Yang, J. (2018). An e-type temperature sensor for upper air meteorology. *Nanotechnology and Precision Engineering*, 1(2), 145–149.
23. Deo, R. C., Şahin, M., Adamowski, J. F., Mi, J. (2019). Universally deployable extreme learning machines integrated with remotely sensed MODIS satellite predictors over Australia to forecast global solar radiation: a new approach. *Renewable and Sustainable Energy Reviews*, 104, 235–261. DOI 10.1016/j.rser.2019.01.009.
24. Yang, J., Liu, Q., Dai, W. (2017). Computational fluid dynamics analysis and experimental study of a low measurement error temperature sensor used in climate observation. *Review of Scientific Instruments*, 88(2), 024902. DOI 10.1063/1.4975591.